Physica Scripta. Vol. 42, 355–358, 1990.

On some Limitations in Interpreting Electron Micrographs*

K. Scheerschmidt and R. Hillebrand

Akademie der Wissenschaften der DDR, Institut für Festköperphysik und Elektronenmikroskopie, 4020 Halle, German Democratic Republic

Received January 4, 1990; accepted February 22, 1990

Abstract

Computer simulations of defocus diffraction contrast and lattice fringe images enable details of electron micrographs of small lattice defects to be interpreted if the electron optical imaging process is included in addition to the interaction between electron beam and crystal. Multi-slice calculations of high-resolution electron microscope images are applied to randomly disturbed silicon structures to evaluate the possibilities and limitations of local structure interpretation. An extension of the iteration procedure is proposed to apply the optical potential concept to eigenvalue system of inelastic-scattered electrons. All three examples given are possibilities of extending the applicability of approximations inherent in theoretical descriptions of electron beam–matter interaction.

1. Introduction

In transmission electron microscopy the nature of small crystal lattice defects can be analysed by the well-established method of diffraction contrast imaging. Additional supporting information can be obtained from lattice fringe images, whereas the significance of high resolution electron microscopy (HREM) in material science investigations consists in its resolving power providing direct and detailed information on the local structural variability at the atomic level.

Though the theoretical image calculation always tends to establish standard rules of interpretation, in the majority of cases a direct and phenomenological analysis of electron micrographs is not possible, and the unambiguous determination of the defect structure with respect to the contrast obtained requires the application of image simulation and matching techniques.

The image is modelled by calculating the electron beam–specimen interaction using a theoretical structure model, and by subsequently considering the electron optical process itself including the aberrations of the microscope. An extensive number of different computer programs have been developed to perform the computations which are all based on the dynamical theory of electron diffraction and Abbe's theory of image formation, respectively. As to the calculation of diffraction contrast images mostly the column approximation is applied and the coupled first-order differential equation system due to the plane or Bloch wave expansion of electron wave function is treated [1].

The HREM image contrast is computed using one of the different multi-slice techniques: their applicability, advantages and unsolved problems are discussed in [2]. The different approximations, e.g., periodic continuation or column approximation, phenomenological description of absorption and inelastic scattering, finite number of diffracted beams and image sampling, limit the applicability of the interpretation techniques. In the following three of them are considered in detail.

2. Defocus diffraction contrast and lattice fringe imaging

Difficulties in applying the above arise, for instance, if extended defects are to be investigated as the column approximation limits the resolvable fine details and the periodic continuation inherent in multi-slice techniques leads to an overlay effect. For sufficiently thin crystals, however, the column approximation is valid, enabling the combination of the calculation of diffraction contrast amplitudes and of the imaging process in the microscope [3] to study defocussed diffraction contrast and lattice fringe images. In [4] this technique is applied to investigate systematically the nature of small prismatic hexagonal dislocation loops of Frank type inclined to the electron beam. Similar to these results, Fig. 1 shows the calculated bright-field, dark-field and lattice fringe contrasts of a spherical precipitate in isotropic materials. The thickness interval of $1.0 \leqslant t/\xi_g \leqslant 1.5$ (ξ_g extinction length) and the depth positions of $0.125 \leqslant t_0/\xi_g \leqslant 1.25$ considered are representative for all contrast features due to the periodicity of the diffraction contrast. The symmetry of the precipitate that is higher than other defect configurations ensures the general classification of the contrast phenomena. The imaging parameters are given in the inset: diffraction vector $\boldsymbol{g}$, incident beam direction $\boldsymbol{e}$, excitation parameter w, effective constraint strain ε, radius of precipitate R_0, spherical aberration C_s, and defocus Δ.

The comparison of the associated micrographs enables the analysis of the lattice fringe distortions (bending, shift, termination) in terms of the phase difference between transmitted and diffracted beams. But, because of the depth-thickness periodicity, the lattice fringe distortions, especially the outward or inward bendings, no longer prove unequivocally the defect nature. Furthermore, the contrast is sensitively influenced by through-focussing and by dynamical excitation conditions. Under fixed diffraction and imaging conditions, however, the phase difference and therefore the fine details of the fringe distortions are directly related to the defect structure assumed. In Fig. 2 the dependence is investigated of bright-field, dark-field and lattice fringe contrasts of a spherical precipitate for $t = 1.125\xi_g$ and $t_0 = 0.125\xi_g$ of Fig. 1, relative to the radius R_T assumed for the homogeneous region of the strain centre. For $R_T = 0$ the spherical precipitate acts as an infinitesimal small point defect singularity with a strength given by the constrained strain ε and the radius R_0, whereas for $R_T = 1$ the complete precipitate is free of strains due to homogeneity but with an unchanged far field. The analysis of the phase-influencing behaviour of lattice defects should therefore facilitate defect structure investigations [5].

---

* Revised short paper presented at the 8th General Conference of the Condensed Matter Division, Budapest, 6–9 April 1988.

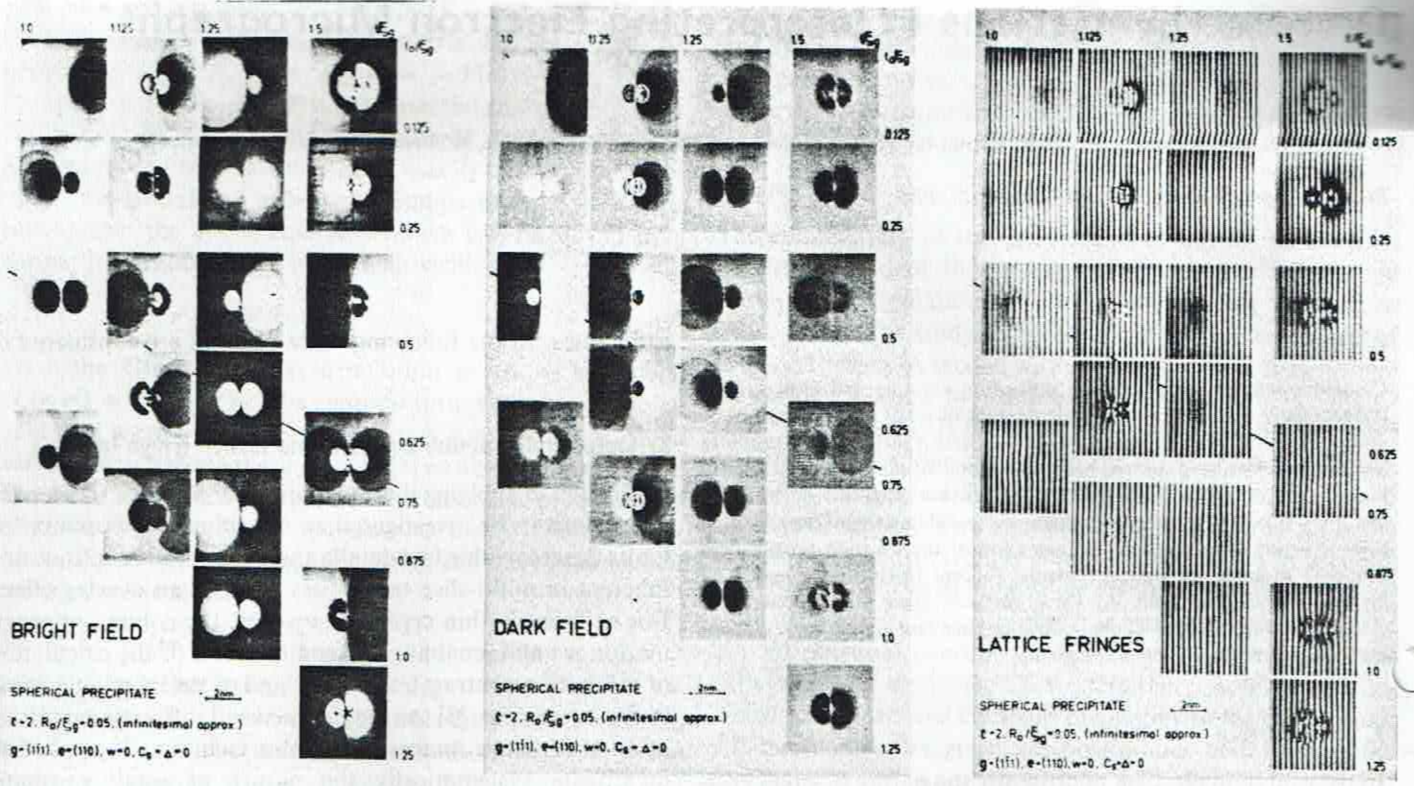

Fig. 1. Calculated bright-field I_{000}, dark-field I_{111} and (111)-lattice fringe contrast of a spherical precipitate as a function of the foil thickness t/ξ_g and the depth position t_0/ξ_g of the defect centre.

3. High-resolution imaging of non-crystalline materials

The application of HREM imaging techniques to non-crystalline materials mainly implies the projection-problem of structures with long-range disorder. Using the multi-slice technique and sufficiently extended supercells for simple amorphized structure models enables the possibilities and limitations of local HREM structure interpretation to be evaluated [6].

Figure 3 shows for example contrast calculations of a sandwich structure consisting of 2 × 2-(110)-silicon supercells (denoted by a) forming the crystalline matrix which is embedded in a different numbers of amorphous slices (types b and c). For slices of type b amorphized cells are applied with different initial random conditions but uniformly distributed disturbances of the atoms of maximum 0.07 nm, whereas for slices of type c a dense random packing of hard spheres is used having a first-order neighbour distance of 0.18 nm. In Figs 3(a) to 3(d) the number of amorphous surface layers rises from two (1b/8a/1b) to eight (4b/2a/4b), and the contrast of the crystalline matrix is increasingly disturbed. This holds for both imaging conditions of $\Delta = -8.7$ nm (upper row), where the crystal structure is preferred using the aberration-free imaging of the matrix, and for $\Delta = 50$ nm (bottom row) with lattice fringe-like contrast, where the random disturbances near the Scherzer focus can better be detected. Fig. 4 shows two defocus series ($\Delta = -8.7, 50, 100$ nm) for a small di-vacancy cluster in silicon. In the upper row only perfect crystalline silicon surrounds the di-vacancy, whereas in the bottom row two amorphized silicon slices are additionally assumed on both surfaces. The slices containing the point defect (denoted by v) are characterized by the potential shown in the insert. For both cases of aberration free focus for the matrix ($\Delta = -8.7$ nm) structure-like images of the crystal are obtained and the position of the cluster is weakly marked. For the virtual lattice fringe-like contrast near the Scherzer focus ($\Delta = 50$ nm) and for higher underfocus the contrast of the point defect cluster is suppressed more or less due to the contrast speckles of the amorphous surface layers.

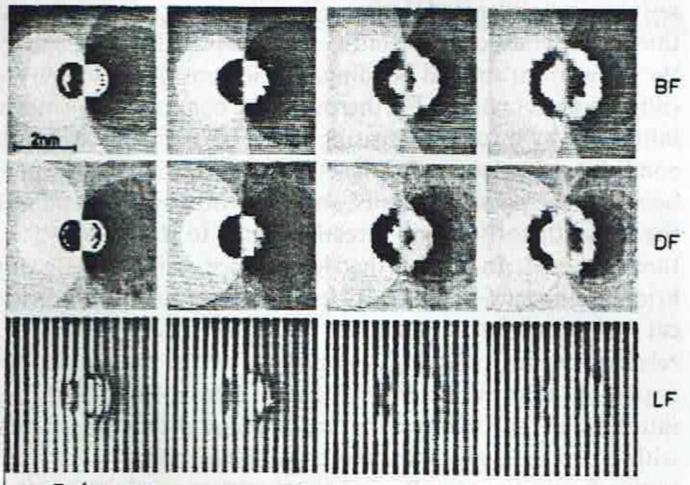

Fig. 2. Bright-field (BF), Dark-field (DF), and Lattice-fringe (LF) images of a spherical precipitate for different radius R_T of the homogeneous strain centre. $g = (111)$, $e = (110)$, $t = 1.125\,\xi_g$, $t_0 = 0.125\,\xi_g$, $\varepsilon = 2$, $R_0 = 0.05\,\xi_g$; $C_s = \Delta = 0$.

Under dark-field imaging conditions local crystal defects markedly appear in the contrast; especially the 3-beam mode $(1\bar{1}1)$, $(1\bar{1}\bar{1})$, (220) has proved to be experimentally advantageous for imaging di-vacancies in (110) silicon layers. Figure 5 shows simulated HREM-micrographs (bottom row) of a 10-slice model under these 3-beam dark-field conditions. The projected potential of the di-vacancy slice is given in the upper row; three di-vacancy slices are surrounded by a per-

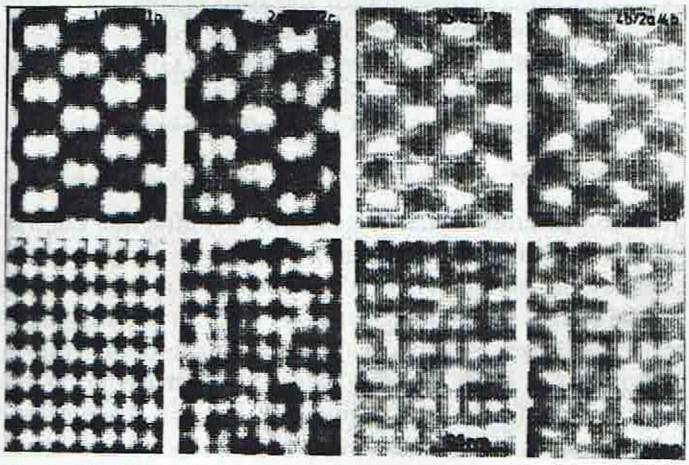

Fig. 3. HREM-simulation of amorphous-crystalline sandwich models (Δ in nm, $V = 100\,\text{kV}$, $C_s = 0.7\,\text{mm}$). Slices: a = 2 × 2-(110)-Si cell, b = amorphized a-type (max 0.07 nm), c = dense random packing of hard spheres.

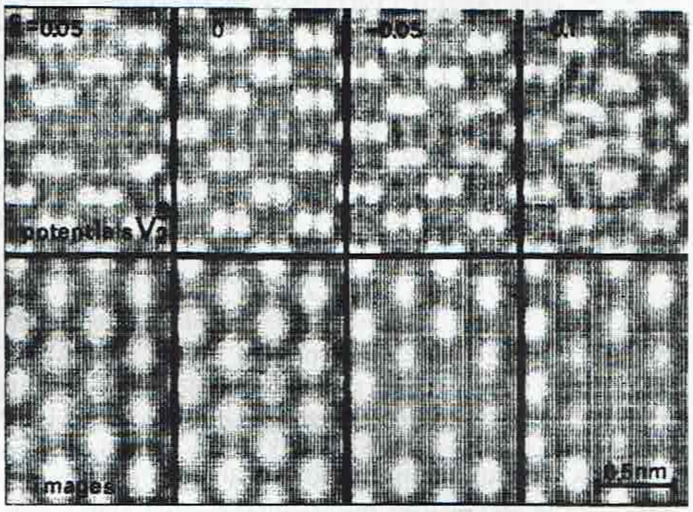

Fig. 5. (110)-silicon tilted 3-beam dark-field images (100 kV) of di-vacancies with relaxation approximated by a spherical precipitate of the misfit ε. Slice sequence: 1b/3a/3v/2a/1b, a = 2 × 2-(110)-Si cell, b = amorphized a-type slice, v = di-vacancy slice (projected potential of v-slice in the upper row).

fect silicon matrix and one amorphous layer at each surface. The constrained strain ε describes the misfit of a coherent precipitate in the approximation of a point defect singularity characterizing the relaxation of the neighbour atoms around the di-vacancy ($\varepsilon < 0$ compression, $\varepsilon > 0$ dilation). The comparison with experiments yields better results for compression centres, and the contrast is only weakly influenced by changing the imaging conditions or applying the surface layers.

Figure 6(a) presents HREM-simulations of a crystalline embryo in an emorphous specimen (top) as well as contrast phenomena of an amorphous microregion in a crystalline matrix (bottom). The models are generated using 4 × 4-(110)-silicon supercells, where the cut-off radius of the sphere discriminating disturbed atoms from undisturbed ones is 0.75 nm. The spherical microregion is placed at 4 inner defect slices in a silicon specimen of $t = 3.8\,\text{nm}$ thickness. According to experimental experience the 100 kV calculations also show that disordered microregions of about 100 atoms may be detected in the vicinity of Scherzer focus even for medium resolution and coherence ($\alpha = 3.3\,\text{nm}^{-1}$, $\delta = 5\,\text{nm}$) considered here. Here amorphous inclusions are imaged with the improved contrast slightly below the Scherzer focus, whereas crystalline embryos are clearly visible slightly above the Scherzer focus.

The experimental micrograph in Fig. 6(b), a HREM cross-sectional image of the interface region of a buried amorphous layer after As$^+$-implantation into ⟨100⟩-silicon, contains ordered regions within the speckled contrast of amorphized silicon, and differently extended amorphized structures relative to the original crystalline silicon.

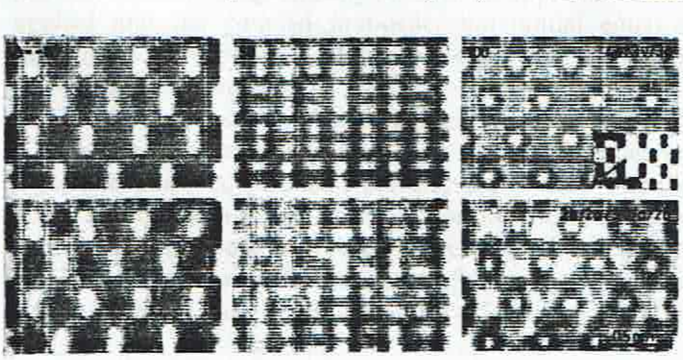

Fig. 4. Simulated HREM defocus series (Δ in nm) of sandwich systems with di-vacancy slices (v), perfect (a) and amorphized (b) 2 × 2-(110)-Si cells; insert: projected potential of a di-vacancy slice; $V = 100\,\text{kV}$, $C_s = 0.7\,\text{mm}$, $\alpha = 7.5\,\text{nm}^{-1}$, $\delta = 1\,\text{nm}$.

4. Inelastically scattered electrons

The Hamiltonian of the Schrödinger equation for a fast electron of total energy E interacting with a crystal can be constructed using $H_e = -\hbar^2/2m\Delta_r$, $H_c = H_c(\boldsymbol{q})$ and $H_i = H_i(\boldsymbol{r}, \boldsymbol{q})$ for the free electron, for the crystal and for the interaction between them, respectively. The assumption that the eigenstates $a_n(\boldsymbol{q})$ with energy ε_n of H_c are known, allows the expansion of the total wave function $\psi(\boldsymbol{r}, \boldsymbol{q}) = \Sigma_n\, a_n(\boldsymbol{q})\, \psi_n(\boldsymbol{r})$ in terms of the crystal eigenstates, where ψ_0 and ψ_n describe the elastic and inelastic scattering, respectively. It follows [7, 8]:

$$(\Delta_r + k_n^2 - H_{nn})\,\psi_n = \sum_{m \neq n} H_{nm}\,\psi_m \qquad (1)$$

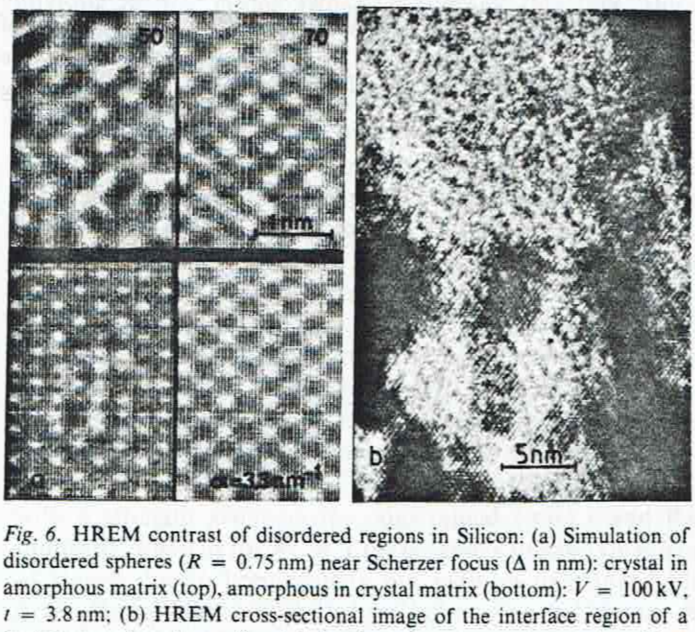

Fig. 6. HREM contrast of disordered regions in Silicon: (a) Simulation of disordered spheres ($R = 0.75\,\text{nm}$) near Scherzer focus (Δ in nm): crystal in amorphous matrix (top), amorphous in crystal matrix (bottom): $V = 100\,\text{kV}$, $t = 3.8\,\text{nm}$; (b) HREM cross-sectional image of the interface region of a buried amorphous layer after As$^+$-implantation at room temperature ($E = 130\,\text{keV}$, $D = 10^{14}\,\text{cm}^{-2}$) into (100)-Silicon (experiment: P. Werner and H. Bartsch).

with the abbreviations $k_n^2 = 2m/\hbar^2(E - \varepsilon_n)$ and $H_{nm} = 2m/\hbar^2 \langle a_n|H_i|a_m\rangle$. The diagonal matrix elements can be approximated by $H_{nn}(\boldsymbol{r}) = H_{00}(\boldsymbol{r}) = -V(\boldsymbol{r}) = -\Sigma_g V_g \exp(-2\pi i \boldsymbol{g}\boldsymbol{r})$, where $2m/\hbar^2 V(\boldsymbol{r})$ is the potential energy, i.e. $V(\boldsymbol{r})$ is the potential usually employed, and V_g are the structure amplitudes. A further assumption is usually made, the inelastic waves are considered to be small compared with the elastic one so that the above equation system can be solved by a formal integration for $n > 0$ which yields

$$\psi_n = \int G_n(\boldsymbol{r}, \boldsymbol{r}')H_{n0}(\boldsymbol{r}')\psi_0(\boldsymbol{r}')\mathrm{d}\boldsymbol{r}' \qquad (2)$$

Here the Greenian G_n as a solution of $(\Delta_r + k_n^2 - H_{nn}) G_n(\boldsymbol{r}, \boldsymbol{r}') = \delta(\boldsymbol{r} - \boldsymbol{r}')$ in the simplest form describes outgoing spherical waves; in [7] the Greenian is constructed of Bloch waves characterizing the crystal. In [8] an absorption corrected Greenian is applied using a special iteration procedure to improve the accuracy of the state vectors by higher-order terms of multiple scattering. For the elastic wave then follows the eigenvalue system

$$(\Delta_r + k_0^2 - H'_{00})\,\psi_0 = 0 \qquad (3)$$

with the so called optical potential H'_{00}.

An extension of the iteration procedure can be realized assuming that $H_{nm} \ll H_{nn}$ holds but without supposing that inelastic scattering is weak. Since the formal integration of the initial differential equations (2) yields an equivalent system of integral equations each inelastic state ψ_n can be treated similar to the elastic one ψ_0 in [8]. It follows an eigenvalue system

$$(\Delta_r + k_n^2 - H'_{nn})\,\psi_n = 0 \qquad (4)$$

for each state ψ_n with an associated optical potential H'_{nn}. Using an approximation analogous to [8] the absorption corrected Greenian contains H'_{nn} instead of H_{nn} and the matrix elements can be written

$$H'_{nm} = H_{nm} + \sum_{l \neq m,n} H_{ml}G_lH_{ln} + \sum_{\substack{l \neq m \\ j \neq m,n}} H_{ml}G_lH_{lj}G_jH_{jn} + \ldots \qquad (5)$$

Consequently, the integral equations (2) are reduced to initial value conditions. Some difficulties (convergence, direction of $\boldsymbol{k}_n$) can be avoided by solving the complete eigenvalue systems (4) including Greenian of outgoing and incoming waves as well as backscattered Bloch-waves [9]. The advantage of this approximation consists in the equivalence of all the eigenvalue systems for constructing the Greenian as well as the different inelastic state vectors.

5. Conclusions

The combination of the calculations of diffraction contrast amplitudes and of the imaging process in the microscope enables the simulation of diffraction contrast and lattice fringe images for studying details of electron micrographs of extended defects. A second way of including three-dimensional distortions is given by using extended supercells in "multislice" calculations. It is obvious that the shift, bending and termination of fringe systems in the micrographs are determined by the phase differences of the diffracted beams due to the crystal defects. Furthermore, the projection effect is the factor which most strongly limits the resolution in imaging distorted structures of long-range disorder. Finally, an extension of the iteration procedure is proposed to apply the optical potential concept to eigenvalue systems of inelastically scattered electrons. This offers the possibility to treat inelastically scattered electrons in analogy to the elastic ones. All three examples given are possibilities of extending the applicability of approximations inherent in theoretical descriptions of electron beam-matter interaction.

References

1. Scheerschmidt, K., in Electron Microscopy in Solid State Physics, (Edited by H. Bethge, J. Heydenreich), p. 535, Elsevier Amsterdam (1987).
2. van Dyck, D., Advances in Electronics and Electron Physics, **65**, 295 (1985).
3. Scheerschmidt, K. and Hillebrand, R., Phys. Status Solidi (a) **91**, 465 (1985).
4. Hillebrand, R., Scheerschmidt, K. and Heydenreich, J., Ultramicroscopy **20**, 465 (1986).
5. Scheerschmidt, K. Hillebrand, R. and Heydenreich, J., Phys. Status Solidi (a) **116**, 123 (1989).
6. Scheerschmidt, K., Hillebrand, R., Heydenreich, J., Optik **77**, 11 (1987).
7. Radi, G., Zeitschr. f. Physik **212**, 146 (1968).
8. Serneels, R., Haentjens, D. and Gevers, R., Phil. Mag. **A42**, 1 (1980).
9. Scheerschmidt, K. and Carl, S. (to be published).